Hearing the dynamical Floquet-Thouless pump of a sound pulse

Ping Hu,[1] Hong-Wei Wu,[1,*] Pengxiang Xie,[1] Yue Zhuo,[1] Wenjun Sun,[1] Zongqiang Sheng,[1] and Yiming Pan[2,†]
[1]*School of Mechanics and Photoelectric Physics, Anhui University of Science and Technology, Huainan 232001, China*
[2]*School of Physical Science and Technology and Center for Transformative Science, ShanghaiTech University, Shanghai 200031, China*

(Received 19 May 2023; revised 7 January 2024; accepted 11 June 2024; published 16 August 2024)

Topological pumps have many implications in physics; for instance, it enables coherent transfer of energy, charge, and spin. However, a topological pump would fail for signal and information transmission since the underlying adiabatic condition is unavoidably violated with rapid modulation. Here, we construct a nonadiabatic pump in a two-color Floquet setting of topological acoustics and demonstrate a dynamical topological pumping for delivering signal pulse in both real time (t) and propagation axis (z, synthetic time). The pulse transfer indicates a direct detection of anomalous topological invariants of periodically driven systems. Using our fabricated acoustic waveguide arrays, we demonstrate a topological pump transport of both continuous and pulsed sound waves, proving the utility of our pump array for dynamical signal transmission and wave manipulation. Our findings can advance both fundamentals and implementations of dynamical topological pumps in driven systems.

DOI: 10.1103/PhysRevB.110.085137

I. INTRODUCTION

Topological pumping was first proposed by Thouless in 1983, when he analyzed a quantized charge motion subject to a slow cyclic modulation of a periodic potential [1,2]. Unlike conventional electronic diabatic pumps, a topological pump allows an electron wave function to flow parametrically from one boundary into the bulk and fully emerge at the opposite boundary after an adiabatic modulation cycle. The pumped charge per cycle has been utilized to investigate topological phases since it provides a direct detection of topological invariants. Thouless pumps have found applications in regulating wave transport in various "wave" systems such as optical [3–8], acoustic [9–13], and elastic waves [14]. For instance, the pump has been demonstrated in photonic Fibonacci quasicrystal [6], acoustic topological lattice [13], and a magneto-mechanical topological insulator [15]. However, adiabatic modulation required by Thouless pumps (to avoid level crossing and scattering between instantaneous eigenstates) poses a significant obstacle for practical applications such as signal transmission. Recent research has shown the possibility of overcoming this constraint in plasmonic waveguides [16], where non-Hermitian engineering is employed to achieve energy transport. Here, we address that, a general dynamical pump framework is required to preserve quantized transport in a temporal pump process, thus avoiding the limitations of adiabatic conditions.

Relaxing adiabatic constraints in topological pumps offers two benefits. First, it provides a method for detecting topological numbers of driven systems. A system when evolved by the drive, usually breaks the adiabatic condition. Thus, constructing a nonadiabatic pump mechanism capable of sensing anomalous topological numbers becomes fundamentally essential. Second, from a practical perspective, nonadiabatic pumps enable the transmission of signals and information over a broad frequency bandwidth. This is particularly advantageous in waveguide-based topological lattices [17] where wave propagation is not limited to being monochromatic or paraxial. Both the real time (t) and the propagation coordinate (z) need to be considered simultaneously, rather than replacing z with t in the quantum-optical analogy [18].

Notably, numerous artificial acoustic microstructures have been constructed to implement the Thouless pump under adiabatic constraints [19,20]. To achieve adiabatic pumping, acoustic topological edge states [21] are generated in acoustic resonators [13] following the Aubry-André-Harper model [11,22]. Recently, a novel approach [12] shows acoustic topological pumping in time by varying the relative position of bilayered metamaterials, leading to the construction of an aperiodic acoustic crystal with a periodically driven phason. In addition, a nonreciprocal topological pump [10] was constructed using spatiotemporally modulated boundary conditions in a time-varying acoustic waveguide system. In response to the growing demand for innovative acoustic wave manipulation, there is a pressing need for a dynamical, robust, and nonadiabatic pump capable of manipulating sound pulse effectively.

Here, we propose a dynamical Floquet-Thouless pump of sound capable of nonadiabatically delivering both acoustic energy and signal in a periodically driven system. Our acoustic waveguide array with small sheets is beneficial for sound signal transmission to confront the difficulty of pumping broad bandwidth sound information. We achieve efficient and robust transmission of an acoustic signal by dynamically broadcasting a sound pulse from one boundary of the array to the other and then receiving it. Remarkably, the temporal pulse pump manifests a direct measurement of topological invariants, surpassing the assumption of wave monochromaticity in

*Contact author: hwwu@aust.edu.cn
†Contact author: yiming.pan@shanghaitech.edu.cn

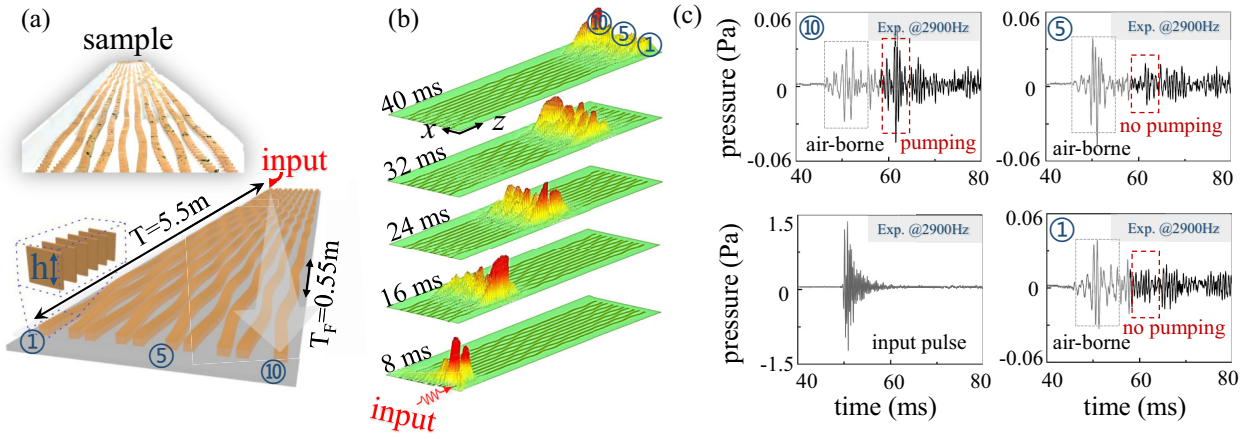

FIG. 1. Setup, simulation, and observation of the dynamical Floquet-Thouless pump of sound pulses. (a) Schematic diagram of a periodically modulated acoustic waveguide array in a two-color Floquet setting. The inset shows a fabricated acoustic array sample aligned by a bunch of sheets of acrylic plates. (b) The near-field FEM simulation of the pulse pump process at different physical times. The input sound has a central frequency of 2950 Hz with a bandwidth of 500 Hz. The movie of the pulse pump is given in the Supplemental Mataerial [28]. (c) The experimental observation of the final output acoustic pulse intensity at different waveguide, corresponding to the first, fifth, and tenth waveguide in the simulation. The input sound pulse has a frequency at 2900 Hz.

topological lattices. Our results validate the accessibility and practicability of our proposed topological pump of signal and information, exceeding the limits of an adiabatic pump for energy or charge.

II. FLOQUET-THOULESS PUMPING FOR ACOUSTIC PULSE

Figure 1(a) depicts our proposed acoustic waveguide array, based on an extended Floquet Rice-Mele model that was first proposed by Pan *et al.* [23], to study the topological pump of anomalous Floquet states. The array consists of ten curved acrylic waveguides with a height of 20 mm and variable widths ranging from 26.6 to 33.4 mm, with a manufacturing error of 0.1 mm. At the top and bottom of the array, smooth, transparent acrylic plates are put in to create a two-dimensional closed space. The soundproof sponge completely surrounds the waveguide array, shielding it from external acoustic disturbance. A sinusoidal signal at 2890 Hz is generated using a signal generator, amplified by a power amplifier, and sent to the first waveguide via a speaker. The sound intensity in the near field of the array is measured using a microphone. The inset shows the experimental array sample.

While the concept of pumping energy of a microwave is conceivable [23], the temporal pumping of sound pulses considering both the physical time (t) and the propagation direction (z) remains intriguing and demanding. To investigate this, we generated a sound pulse (2950 Hz center frequency, 500 Hz bandwidth) at the first waveguide. Figure 1(b) illustrates simulation results of the acoustic pressure field distribution as the pulse is pumped through the array over a real time range of 8–40 ms. Notably, we observed a pump cycle of $T_p = 32$ ms, corresponding to the design adiabatic length of $T = 5.5$ m. Five distinct steps of the pulse pumping process at different real times are visualized.

To further validate the Floquet-Thouless pump, we performed experimental measurements. A 2900 Hz acoustic pulse is launched at the initial end of the waveguide, and the received signal is analyzed at positions of the first, fifth, and tenth waveguides [Fig. 1(c)]. As expected, the majority of the pulse is collected from the tenth waveguide. Notably, during pulse propagation, a fraction of the signal travels through the air and is captured by the microphone [gray boxes in Fig. 1(c)], while the rest is successfully pumped through the structure to the end of the array. We notice that the incident sound pulses are temporal in real time, as the pulses evolve along the propagation direction (z) in a manner akin to how they would over time (t). Thus, in the quantum-optical analogy, this pulse is also "temporal" in z.

To comprehend the temporal pump dynamics in the array, we must go deep into the full form of the acoustic wave equation. The incident wave is coupled into the waveguide forming a spoof acoustic surface wave propagating along the z direction. In our setup [Fig. 1(a)], sound propagation dynamics are described by a single-variable acoustic wave equation in terms of the sound pressure fluctuation (p),

$$\nabla^2 p - \frac{1}{c_0^2}\frac{\partial^2 p}{\partial t^2} + \frac{\delta}{c_0^4}\frac{\partial^3 p}{\partial t^3} = -\frac{\gamma}{\rho_0 c_0^4}\frac{\partial^2 p^2}{\partial t^2}. \tag{1}$$

This equation is known as the Westervelt equation [24], with $c_0 = \sqrt{\partial p/\partial \tilde{\rho}}$ being the speed of sound from the first-order term of the Taylor expansion of the equation of state $p = p(\tilde{\rho})$, and γ being the nonlinearity coefficient from the second-order expansion. δ represents sound diffusivity induced by viscosities and heat. Given the weak small-amplitude pressure fluctuation (p) in our setting, the linearization of Eq. (1) suffices to describe sound propagation (i.e., $\gamma = 0$). See the simulation result in Fig. 1(b) for nontrivial temporal dynamics when the real time t is retained.

To determine the topological protection of the pulse pumping, we decompose the linearized Westervelt equation into a topological tight-binding model under monochromaticity and paraxiality criteria. Considering a monochromatic pressure wave $p = \tilde{p}e^{-i\omega t}$ with frequency ω, propagating mainly along the z direction, we approximate it as $\tilde{p} = \tilde{p}_z(x, z)e^{ik_z z}$ with

wave number k_z. By inserting this ansatz into Eq. (1), we derive a paraxial wave equation in terms of $\tilde{p}_z$:

$$i\partial_z \tilde{p}_z = -\frac{\partial_x^2}{2k_z}\tilde{p}_z - \frac{1}{2k_z}\left(\frac{\omega^2}{c_0^2} - k_z^2 + i\frac{\omega^3\delta}{c_0^4}\right)\tilde{p}_z, \qquad (2)$$

where only the two-dimensional space (x, z) is considered, and the second derivative of z is disregarded under the paraxial condition. The acoustic wave propagation becomes equivalent to the Schrödinger equation for longitudinal monochromatic sound pressure when treating the propagation direction z as a synthetic time, using the quantum-optical analogy [25]. Notice that the real time t is embedded in the parameters associated with the sound frequency ω. Detailed derivations of the acoustic Schrödinger equation are given in the Appendix, Sec. 3.

Assuming weak coupling between the curved waveguides, where the overlap integrals vanish for $|m-n| > 1$, $C_{n,m} = 0$, we arrive at the tight-binding-approximated (TBA) Schrödinger equation, considering only nearest-neighbor couplings:

$$i\partial_z \psi_i = \beta_i(z)\psi_i + \kappa_{i+1,i}(z)\psi_{i+1} + \kappa_{i-1,i}(z)\psi_{i-1}, \qquad (3)$$

where $\beta_i(z) = \beta_0 + \Delta\beta(z)(-1)^i$ with β_0 being the averaged complex propagation constant and $\Delta\beta(z) = \Delta\beta_0 \sin(\Omega z)$ the staggered on-site potential. Additionally, $\kappa_{i+1,i} = \kappa_0 + \Delta\kappa(z)(-1)^i$ with κ_0 being the averaged coupling strength and $\Delta\kappa(z) = \Delta\kappa_0 \cos(\Omega_F z)\cos(\Omega z)$ the staggered coupling strength. Notice that both on-site potentials and coupling strengths depend on the real frequency ω of the monochromatic sound.

In our Floquet setting, two modulation frequencies are deployed on the staggered couplings: Floquet frequency $\Omega_F = 2\pi/T_F$ (Floquet cycle T_F) and adiabatic frequency $\Omega = 2\pi/T$ (adiabatic cycle T). Only adiabatic modulation is applied to the staggered on-site potential $\Delta\beta(z)$. The modulation frequencies and cycles relate to the synthetic time z of the unit in length, not real time t. To achieve an anomalous topological pumping, we require two driven frequencies in two-color Floquet engineering [23]: the first drive establishes an anomalous Floquet steady state, and the second drive steers it in an adiabaticlike manner. The topological number associated with the opening of an anomalous π gap was discussed [23]. To be specific in our two-color setting, the condition $T \gg T_F$ is required; the adiabatic cycle is larger than the Floquet cycle. Here, we simulate the condition $T = 10T_F = 5.5$ m [Fig. 1(a)], with the propagation constants and the coupling strengths of the array discussed detailed in Fig. 5 in the Appendix.

In conventional notation, the adiabatic condition necessitates an extremely slow evolution of the system in time t, ensuring it remains within the instantaneous eigenstates without scattering into adjacent states. In the framework of the quantum-optical analogy (where t is analogous to z), adiabaticity enforces a slow evolution along the propagation axis z (the synthetic time). In our setup, the Floquet-Thouless pump for sound pulses clearly violates the adiabatic condition in two aspects: in real time t and synthetic time z. The adiabaticity in t is compromised due to pulse propagation encompassing a range of sound frequencies, while the adiabatic condition for z is likewise disrupted by rapid Floquet modulation in the curved waveguide configuration. It is noteworthy that synthetic time z for the Floquet pumping presented in this work is different with a conventional spatial pump. However, the spatial pump in propagation direction is utilized to mimic the Floquet pump in real time.

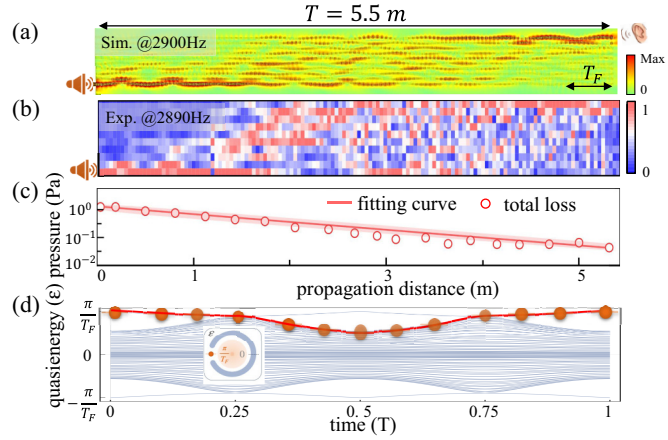

FIG. 2. Observation of the Floquet-Thouless pump in acoustic waveguide arrays. (a) The FEM simulation of the pump on the array. (b) The measured near-field distribution of the normalized acoustic field at a frequency of 2890 Hz. (c) The total intensity decreases exponentially as a function of the propagation distance due to the sound diffusivity. (d) The nonadiabatic pump channel is constructed in the quasienergy spectrum based on our Floquet-Thouless pump model. The inset shows the pumped topological number, corresponding to the anomalous π modes.

III. NEAR-FIELD MEASUREMENT

To demonstrate the near-field distribution of the Floquet-Thouless pump, we design a specific acoustic array and compare simulation results with experiments, as shown in Fig. 2. According to practical waveguide structure (see Appendix, Sec. 2), we estimate the coupling amplitudes $\kappa_0 \approx 5.236$ (m^{-1}), $\Delta\kappa \approx 0.897$ (m^{-1}) and the on-site potentials $\beta_0 \approx 65.62$ (m^{-1}), $\Delta\beta_0 \approx 11.17$ (m^{-1}). Figure 2(a) illustrates our finite-element simulation of the pumping process. When the sound wave with a frequency of 2900 Hz is ejected from the first waveguide, the acoustic energy of the sound wave is mostly pumped into the tenth waveguide after a cycle of T. Figure 2(b) shows the observed pump process, as the sound travels from the first waveguide to the tenth, after completing a cycle of T, consistent with our theoretical analysis and simulation of the nonadiabatic pump model. Incidentally launching the wave from from the fifth waveguide does not excite the pump channel, demonstrating the inefficiency of pumping via the nontopological Floquet bulk (see Appendix, Fig. 6).

A particular emphasis is placed on the sound attenuation along acoustic waveguides. To provide a clear pattern of the acoustic pump dynamics, we normalize the experimental data at each propagation distance, eliminating attenuation effects. The total damped intensity in terms of the propagation distance is shown in Fig. 2(c), where red circles represent the

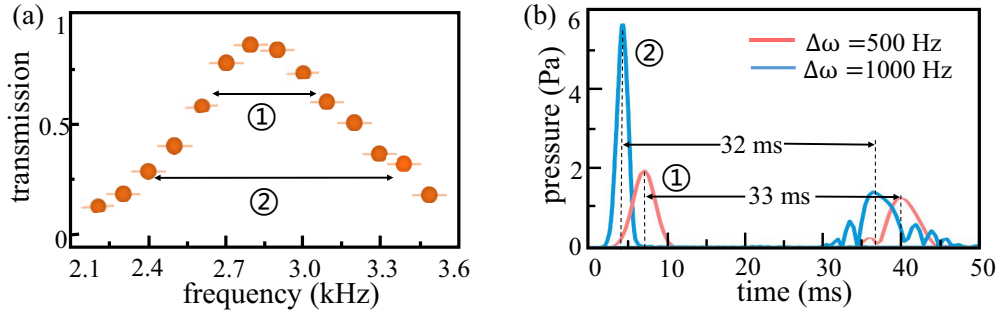

FIG. 3. Transmission and dispersion of pumping acoustic pulses. (a) Transmission rate of monochromatic acoustic waves at frequencies ranging from 2200 to 3500 Hz. The optimum transmission of the pump channel is close to one at 2850 Hz. (b) Two sound pulses are temporally pumped, having a bandwidth of 500 Hz (red curve) and 1000 Hz (blue curve), respectively, in the central frequency of 2950 Hz.

sum of the acoustic wave magnitudes in each column along propagation, fitted to a logarithmic linear curve. This curve indicates rapid decay of acoustic energy loss during propagation. Therefore, we can safely say that the sound attenuation does not ruin the pump pattern. Additionally, we examine that the experimental data and simulations matched well at the output of the last Floquet cycle (see Appendix, Fig. 7).

The topological number pumped in our Floquet-Thouless pump shares similarities with the adiabatic pump. For a detailed comparison of pumping zero modes and π modes, see the Appendix, Figs. 8 and 9. When the Floquet driving (T_F) is removed, the Floquet Rice-Mele model [Eq. (3)] transforms into its adiabatic version [26], capable of pumping zero modes [27]. Nevertheless, our Floquet-Thouless model facilitates the transfer of anomalous π modes inherent to periodically driven systems. Furthermore, we can clarify our pump model by comparing it to conventional quantum pumping, such as the Aubry-André-Harper (AAH) model. The AAH model is characterized as a quasiperiodic and adiabatic model, whereas our Floquet-Thouless pump displays periodic behavior but is nonadiabatic. Figure 2(d) shows the quasienergy spectrum featuring an anomalous π mode, elucidating the construction of a nonadiabatic pump channel in a two-color Floquet setting.

IV. DISCUSSIONS

We investigate the pump transmission rate of our acoustic array by sending a continuous sound wave. Figure 3(a) shows that the array maintains a high transmission rate across a wide frequency range. The maximum rate reaches 86.5% at 2850 Hz, while the lowest rate remains at 13.9% at 2200 Hz. This finding provides insight into the temporal pulse pump observed in Fig. 1(b).

The pulse, comprising monochromatic components with different pump transmission, experiences variations in the coupling strength and on-site potentials with the sound frequency. This variation in parameters is likely to distort the pulse shape during propagation by altering the quasienergy band dispersion. However, our setup, regardless of the quasienergy band dispersion, maintians a fixed pumping cycle at T. This holds true as long as the coupling configurations support a topological pump channel in the spectrum [see the band structure in Fig. 2(d)]. Consequently, our pump effectively preserves signal pulse profiles after one propagation cycle, demonstrating its effectiveness in signal transmission.

To evaluate the transmission performance for different pulse durations, we generate pulses with a center frequency of 2950 Hz and bandwidths of 500 and 1000 Hz. Figure 3(b) depicts pulse pumping results after a propagation time T_p = 32 ms for the bandwidth 1000 Hz, T_p = 33 ms for the bandwidth 500 Hz. The broad pulse is effectively pumped while maintaining reasonable signal shape fidelity at a high level. In contrast, the narrow pulse experiences severe waveform distortion, consistent with the lower transmission rate in Fig. 3(a). Importantly, this distortion is attributed to transmission efficiency rather than band dispersion. Thus, achieving coherent signal pulse pumping in our array requires a relatively smooth and frequency-independent transmission rate.

Figure 4 compares the efficiency of the Floquet-Thouless pump and the adiabatic pump, with simulations conducted across various sound frequencies and structural parameters. The Floquet-Thouless pump exhibits effectiveness at both low and high frequencies, enabling nonadiabatic signal transfer and outperforming the adiabatic pump. Increasing the number of Floquet cycles in a fixed adiabatic cycle enhances nonadiabatic transmission efficiency at high frequencies, as evidenced at 3700 Hz [Fig. 4(b) and Appendix Fig. 10]. Constraints on sound wave propagation in the array manifest at low frequencies due to mode mismatch, while higher frequencies encounter limitations imposed by the cutoff frequency, resulting in leakage into free space. However, the anomalous π mode lies in its ability to serve as a versatile platform for carrying higher-frequency signals during the nonadiabatic pump process—a capability not realized in conventional pumps [see Fig. 4(c)]. The physical mechanism is that the Floquet modulated waveguides provide more chances to couple and pump the sound in our Floquet-Thouless pump. The detailed discussions are presented in the Appendix, Sec. 9. Therefore, the Floquet-Thouless pump allows for more efficient signal and energy transfer across a broader frequency regime, exceedingly released from the adiabatic constraint.

Direct measurement of the topological number in our system relies on the temporal pumping of the signal, distinguishing it from the conventional measurement based on steady-state pumping of plane waves (continuous wave). While steady-state measurements involve transmittance determination, temporal measurements require integration in the time domain. Utilizing a temporal pulse pumping process offers a more intuitive approach to identify and quantify the

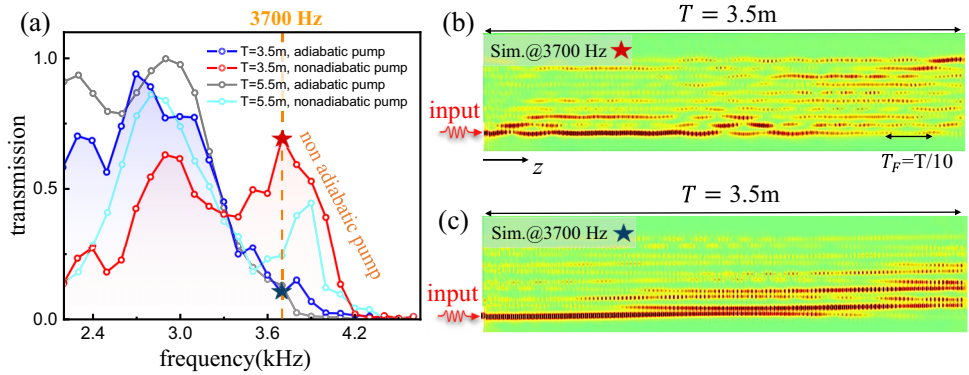

FIG. 4. Peer advantage of the Floquet-Thouless pump efficiency at high-frequency regime. (a) The transmission of adiabatic and nonadiabatic pumps for different settings with adiabatic cycles $T = 3.5$ and 5.5 m, respectively. The Floquet cycles correspond to $T_F = T/10$ for Floquet-Thouless pumps (red and cyan curves). (b), (c) The near-field simulations for nonadiabatic and adiabatic pumps at frequency $f = 3700$ Hz.

topological invariant. Additionally, robustness against defects was thoroughly assessed in the Appendix, Figs. 11 and 12.

V. CONCLUSION

In short, we have constructed and observed a dynamical Floquet-Thouless pump in an acoustic waveguide array with two-color Floquet modulations. Through extensive simulations and experiments, surpassing the quantum-optical analogy, we achieved a nonadiabatic dynamical topological pumping of both continuous and pulsed sound waves. Our findings of pumping signals and information open up a new avenue for advanced acoustic and optical wave manipulation in topological lattices, with potential applications in wavelength division multiplexing and data transmission.

ACKNOWLEDGMENTS

This work was supported by the Natural Science Foundation of the Higher Education Institutions of Anhui Province, China (Grant No. 2022AH040114) and the University Synergy Innovation Program of Anhui Province (Grant No. GXXT-2022-015). Y.P. is supported by the National Natural Science Foundation of China (Grant No. 2023X0201-417).

The authors declare no competing financial interests.

APPENDIX

1. Numerical simulations

The finite-element simulations for this work were performed using the commercial software COMSOL MULTIPHYSICS. Simulation by the acoustic module and frequency domain calculations were used to obtain a stable sound pressure field. In the simulation, the acoustic impedance between the waveguides sheet and air is large, thus the sheet region is set as an interior hard boundary and the peripheral environment of the structure is set as a plane wave radiation boundary condition. The sound pressure field of the tenth Floquet cycle of the tenth waveguide and the sound pressure field of the first Floquet cycle of the first waveguide are integrated separately, and the transmission is derived after the ratio. Our acoustic pulse signal is obtained from the acoustic module in time domain calculation, a probe is placed in the middle of the first waveguide incident port and the tenth waveguide end sheet spacer, respectively, and the sound pressure intensity is recorded to obtain the results in the main text.

2. Sample preparation and acoustic field measurements

The height of the small sheets comprising the waveguide are uniformly 20 mm and their thickness is 2 mm, while the width variation of these sheets in an adiabatic cycle is between 26.6 and 33.4 mm, with the manufacturing error being 0.1 mm. Smooth, transparent acrylic plates with big scales are placed at the top and bottom of the waveguide array to create a two-dimensional closed environment. Then, the waveguides are put in an enclosed environment with a temperature of 20 °C, an air density of 1.21 kg/m^3, and a sound speed of 343 m/s, and are surrounded by a sound insulation sponge. The overall dimensions of the array are 5.5 m in length and 0.65 m in breadth. We use a signal generator (AFG1022, Tektronix) to generate a sinusoidal wave signal, which is then amplified by a power amplifier (CPA2400, SinoCinetech) to drive the speaker facing the first waveguide. The microphone (378B02, PCB Piezotronics) is then used to scan the waveguide array and record its sound pressure intensity at each point.

3. Derivation from Westervelt equations to TBA Schrödinger equation

We would like to derive the governing wave equation for the sound propagation in our topological acoustic lattice composed of acrylic sheets in the air at room temperature ($T = 20^\circ$C). We suppose that our acoustic lattice is an isotropic and perfectly elastic, yet spatially inhomogeneous medium. There are three primary variables that describe acoustic dynamics [24]: the particle velocity $\mathbf{u}$, the mass density ρ, and the pressure P. As the three variables have values that fluctuate around a mean, we can take the small-amplitudes assumption. This assumption indicates that they are typically decomposed into the average values, and fluctuating components, in which the particle velocity is small, $\boldsymbol{u} = \boldsymbol{u}_0 + \tilde{\boldsymbol{u}}$, and there are only

small perturbations (fluctuations) to the equilibrium density and pressure, $\rho = \rho_0 + \tilde{\rho},\ P = P_0 + p$. For our acoustic lattice system, we assume the mean value of the velocity is zero, $\boldsymbol{u}_0 = 0$, the ambient density of the undisturbed air is $\rho_0 = 1.21 kg/\mathrm{m}^3$, and the ambient pressure of the undisturbed air is $P_0 = 1$ atm.

Essentially, the acoustic wave is a pressure fluctuation. A change in local pressure leads to the immediate compression of fluid, resulting in subsequent pressure changes. Our acoustic lattice propagates a sound wave as a result of this mechanism. Therefore, instead of considering the full equations of the three variables, we just discuss the single-variable acoustic wave equation for the sound pressure fluctuation (p), which is given by the Westervelt equation:

$$\nabla^2 p - \frac{1}{c_0^2}\frac{\partial^2 p}{\partial t^2} + \frac{\delta}{c_0^4}\frac{\partial^3 p}{\partial t^3} = -\frac{\gamma}{\rho_0 c_0^4}\frac{\partial^2 p^2}{\partial t^2}, \tag{A1}$$

where $c_0 = \sqrt{\partial p/\partial \tilde{\rho}}$ is the speed of sound from the first-order term of the Taylor series expansion of the equation of state $p = p(\tilde{\rho})$, and γ is the nonlinearity coefficient from the second-order term of the Taylor series expansion. The symbol δ is the sound diffusivity that has two contributions from the viscosities and heat conditions. The derivations of the Westervelt equation from the equations of motion, continuity equation, and constitutive equation can be found in Ref. [24]. Our starting point is the Westervelt equation, from which we would derive the Schrödinger-like coupled-mode equations.

To further simplify the preceding equation, we must take into account the specific configuration of the acoustic lattice. The first is that the acoustic nonlinearity can be disregarded ($\frac{\partial^2 p^2}{\partial t^2} \approx 0$) since the small-amplitude pressure is weak, and the linearization of the equation adequately describes the sound propagation,

$$\nabla^2 p - \frac{1}{c_0^2}\frac{\partial^2 p}{\partial t^2} + \frac{\delta}{c_0^4}\frac{\partial^3 p}{\partial t^3} = 0. \tag{A2}$$

Second, we simplify this linear Westervelt equation by the slow-varying envelope approximation. Consider a monochromatic pressure wave $p = \tilde{p}e^{-i\omega t}$ with the frequency ω, so that the wave equation is obtained:

$$\nabla^2 \tilde{p} + \left(\frac{\omega^2}{c_0^2} + i\frac{\omega^3 \delta}{c_0^4}\right)\tilde{p} = 0. \tag{A3}$$

Then, we assume the sound pressure mainly propagates along the z direction, thus we can approximate the pressure as $\tilde{p} = \tilde{p}_z(x, y, z)e^{ik_z z}$ with the wave number k_z. We calculate each term in Eq. (A3) and present the procedure in the following:

$$\begin{aligned}
\nabla^2 \tilde{p} &= \left(\partial_x^2 + \partial_y^2 + \partial_z^2\right)\tilde{p}_z(x, y, z)e^{ik_z z} \\
&= e^{ik_z z}\left(\partial_x^2 + \partial_y^2 + \partial_z^2 + 2ik_z\partial_z - k_z^2\right)\tilde{p}_z(x, y, z) \\
&= e^{ik_z z}\left(\partial_x^2 + \partial_y^2 + 2ik_z\partial_z - k_z^2\right)\tilde{p}_z(x, y, z), \\
\left(\frac{\omega^2}{{c_0}^2} + i\frac{\omega^3 \delta}{{c_0}^4}\right)\tilde{p} &= e^{ik_z z}\left(\frac{\omega^2}{{c_0}^2} + i\frac{\omega^3 \delta}{{c_0}^4}\right)\tilde{p}_z(x, y, z),
\end{aligned}$$

where, in the last step of the first expression, we take the slow-varying envelope approximation, $|\partial_z^2 \tilde{p}_z| \ll |2ik_z\partial_z \tilde{p}_z|$. Therefore, we obtain the paraxial wave equation

$$i\partial_z \tilde{p}_z = -\frac{\left(\partial_x^2 + \partial_y^2\right)}{2k_z}\tilde{p}_z - \frac{1}{2k_z}\left(\frac{\omega^2}{{c_0}^2} - k_z^2 + i\frac{\omega^3 \delta}{c_0^4}\right)\tilde{p}_z. \tag{A4}$$

In the quantum-optical analogy ($z \to t$), the acoustic wave propagation along the z direction is described by the Schrödinger-type paraxial equation for the longitudinal monochromatic sound pressure. In this sense, the evolution of a sound beam in space resembles the wavefunction of an electron, with z replacing the real time t. The first term in the right-hand side of Eq. (A4) mimics the kinetic energy term, while the second term mimics the potential term [$V(x, y, z) = -\frac{1}{2k_z}(\frac{\omega^2}{{c_0}^2} - k_z^2 + i\frac{\omega^3\delta}{c_0^4})$] in the Schrödinger equation.

Now, let us derive the coupled-mode equations from the paraxial wave equation of the Schrödinger type, Eq. (A4). Notice that the speed of sound $c_0 = \sqrt{\partial p/\partial \tilde{\rho}}$ varies depending on the substance; for instance, in air $c_{0,\mathrm{air}} = 343\,\mathrm{m/s}$, whereas in an acrylic sheet of polymethyl methacrylate $c_{0,\mathrm{acr}} = 1430\,\mathrm{m/s}$. We investigate the periodic distribution of these acrylic sheets in space; the modulation of speed of sound in the array of location (x, z), is then analytically determined:

$$c_0 = c_0(x, z) = \begin{cases} c_{0,\mathrm{air}}, & (x, z) \in \Omega_{\mathrm{air}} \\ c_{0,\mathrm{acr}}, & (x, z) \in \Omega_{\mathrm{acr}}. \end{cases} \tag{A5}$$

For our acoustic lattice configuration, we only consider the two dimensions of the space (x, z). Notice that in our COMSOL MULTIPHYSICS finite-element-method (FEM) simulation, we set the rigid boundary for sound pressure in solids for replacing the acrylic sheets; hence, the speed of sound in the region Ω_{acr} occupied by these sheets is approximately close to infinity.

Let us examine the governing equation [Eq. (A4)]. Considering the periodicity of the sound speed $c_0 = c_0(x, z)$ [Eq. (A5)], we can consider that the potential term is given by

$$V(x, z) = -\frac{1}{2k_z}\left(\frac{\omega^2}{c_0^2} - k_z^2 + i\frac{\omega^3 \delta}{c_0^4}\right) = \sum_n V_0[x - x_n(z)], \tag{A6}$$

where x_n is the location of the nth curved acoustic waveguide in an array and the center trajectory of the waveguide is z dependent, $x_n = x_n(z)$. V_0 is the fundamental potential of the single curved acoustic waveguide.

On each curved waveguide, we assume that the fundamental acoustic guiding modes are given by $W_0(x - x_n(z),\ z)$ (see Supplemental Material, movie V-6 [28]; the cw guiding wave in a curved waveguide), which can be utilized as a normalized basis for constructing the Wannier functions. Therefore, the longitudinal monochromatic sound pressure $\tilde{p}_z$ can be decomposed as follows:

$$\tilde{p}_z = \sum_n \psi_n(z)\, W_0(x - x_n(z),\ z) = \sum_n \psi_n W_{0,n}. \tag{A7}$$

Substituting Eq. (A7) into Eq. (A4), let us perform the following calculations:

$$
\begin{aligned}
i\partial_z \tilde{p}_z &= \sum_n (i\partial_z \psi_n)\, W_{0,n} + \psi_n (i\partial_z W_{0,n}),\\
-\frac{\partial_x^2}{2k_z}\tilde{p}_z &= \sum_n \psi_n \left(-\frac{\partial_x^2}{2k_z} W_{0,n}\right)\\
&\left[-\frac{1}{2k_z}\left(\frac{\omega^2}{c_0^2} - k_z^2 + i\frac{\omega^3\delta}{c_0^4}\right)\right]\tilde{p}_z\\
&= \left[-\frac{1}{2k_z}\left(\frac{\omega^2}{{c_0}^2} - k_z^2 + i\frac{\omega^3\delta}{{c_0}^4}\right)\sum_n \psi_n W_{0,n}\right].
\end{aligned}
$$

so that the wave equation is given by

$$
\begin{aligned}
\sum_n (i\partial_z \psi_n)\, W_{0,n} = \sum_n -\psi_n &\left(i\partial_z W_{0,n} + \frac{\partial_x^2}{2k_z} W_{0,n}\right)\\
&- \frac{1}{2k_z}\left(\frac{\omega^2}{{c_0}^2} - k_z^2 + i\frac{\omega^3\delta}{c_0^4}\right)\sum_n \psi_n W_{0,n}.
\end{aligned}
$$

We take the integration by $\int dx\, W_{0,m}^*$ on the left-hand side of the equation,

$$
\begin{aligned}
&\int dx\, W_{0,m}^* \left(\sum_n (i\partial_z \psi_n) W_{0,n}\right)\\
&= \sum_n (i\partial_z \psi_n) \int dx\, W_{0,m}^* W_{0,n}\\
&= \sum_n (i\partial_z \psi_n) \int dx\, W_0^*(x - x_m(z),\ z) W_0(x - x_n(z),\ z)\\
&= \sum_n (i\partial_z \psi_n)\delta_{m,n} = i\partial_z \psi_m,
\end{aligned}
$$

where we use the orthogonality of the Wannier basis. Using the same trick, we also simplify the wave equation and obtain

$$
i\partial_z \psi_m = \sum_n C_{n,m}\psi_n. \tag{A8}
$$

We take the integration by $\int dx\, W_{0,m}^*$ on the right-hand side of the equation,

$$
\begin{aligned}
&\int dx\, W_{0,m}^* \left[\sum_n -\psi_n \left(i\partial_z W_{0,n} + \frac{\partial_x^2}{2k_z} W_{0,n}\right) - \frac{1}{2k_z}\left(\frac{\omega^2}{c_0^2} - k_z^2 + i\frac{\omega^3\delta}{c_0^4}\right)\psi_n W_{0,n}\right]\\
&= \sum_n \left[-\int dx\, W_{0,m}^* \left(i\partial_z W_{0,n} + \frac{\partial_x^2}{2k_z} W_{0,n}\right) - \frac{1}{2k_z}\left(\frac{\omega^2}{c_0^2 - k_z^2 + i\frac{\omega^3\delta}{c_0^4}}\right)\int dx\, W_{0,m}^* W_{0,n}\right]\psi_n\\
&= \sum_n \left[-\int dx\, W_{0,m}^* \left(i\partial_z + \frac{\partial_x^2}{2k_z}\right) W_{0,n} - \frac{1}{2k_z}\left(\frac{\omega^2}{c_0^2} - k_z^2 + i\frac{\omega^3\delta}{c_0^4}\right)\delta_{m,n}\right]\psi_n = \sum_n C_{n,m}\psi_n.
\end{aligned}
$$

Then, we obtain the coupling coefficients between the acoustic waveguides

$$
C_{n,m} = -\frac{1}{2k_z}\left(\frac{\omega^2}{c_0^2} - k_z^2 + i\frac{\omega^3\delta}{c_0^4}\right)\delta_{m,n} - \int dx\, W_{0,m}^* \left(i\partial_z + \frac{\partial_x^2}{2k_z}\right) W_{0,n}. \tag{A9}
$$

Assuming that the coupling between the curved waveguides is weak, the overlap integrals vanish for $|m-n| > 1$, i.e., $C_{n,m} = 0$. In other words, we disregard the high-order couplings except for the nearest-neighboring coupling. Consequently, we arrive at the tight-binding-approximated Schrödinger equation

$$
\begin{aligned}
i\partial_z \psi_m &= \sum_n C_{n,m}\psi_n\\
&= C_{m,m}\,\psi_m + C_{m+1,m}\,\psi_{m+1} + C_{m-1,m}\,\psi_{m-1}\\
&= \beta_m(z)\psi_m + \kappa_{m+1,m}(z)\psi_{m+1} + \kappa_{m-1,m}(z)\psi_{m-1},
\end{aligned} \tag{A10}
$$

where the complex propagation constant and the nearest-neighboring coupling coefficients are explicitly given by

$$
\begin{aligned}
\beta_m(z) = -\frac{1}{2k_z}&\left(\frac{\omega^2}{c_0^2} - k_z^2 + i\frac{\omega^3\delta}{c_0^4}\right)\\
&- \int dx W_{0,m}^* \left(i\partial_z + \frac{\partial_x^2}{2k_z}\right) W_{0,m},
\end{aligned}
$$

$$
\begin{aligned}
\kappa_{m+1,m}(z) &= -\int dx\, W_{0,m}^* \left(i\partial_z + \frac{\partial_x^2}{2k_z}\right) W_{0,m+1},\\
\kappa_{m-1,m}(z) &= -\int dx\, W_{0,m}^* \left(i\partial_z + \frac{\partial_x^2}{2k_z}\right) W_{0,m-1}.
\end{aligned}
$$

We rewrite the TBA Schrödinger equation in abbreviated form:

$$
i\partial_z \psi_i = \beta_i(z)\psi_i + \kappa_{i+1,i}(z)\psi_{i+1} + \kappa_{i-1,i}(z)\psi_{i-1}. \tag{A11}
$$

Taking into account our specific setup of the acoustic waveguide array [see Fig. 1(a) in the main text], we may design the coupling coefficients and propagation constant:

$$
\begin{aligned}
\beta_i &= \beta_0 + (-1)^i \Delta\beta(z),\\
\kappa_{i+1,i} &= \kappa_0 + \Delta\kappa(z)(-1)^i,\\
\kappa_{i-1,i} &= \kappa_0 + \Delta\kappa(z)(-1)^{i-1},
\end{aligned}
$$

where $\beta_0 = (\beta_r - i\frac{\alpha}{2})$ is the averaged complex propagation constant and κ_0 is the averaged coupling strength between the waveguides. Note that α is the attenuation factor relating to the sound diffusivity (δ) as presented in the Westervelt

equation (A1). The staggered terms are provided by $\Delta\beta(z) = \Delta\beta_0 \sin(\Omega z)$, $\Delta\kappa(z) = \Delta\kappa_0 \cos(\Omega_F z)\cos(\Omega z)$, in which the modulation [the Floquet frequency $\Omega_F = 2\pi/T_F$ (corresponding to Floquet cycle T_F) and the adiabatic frequency $\Omega = 2\pi/T$ (corresponding to adiabatic cycle T)] are introduced by acoustic waveguide fabrication.

Compared to the second quantization formulation of Eq. (A11), the corresponding TBA Hamiltonian is obtained:

$$H = \sum_i [\beta_0 + \Delta\beta(z)(-1)^i] c_i^\dagger c_i + \sum_i [\kappa_0 + \Delta\kappa(z)(-1)^i] c_{i+1}^\dagger c_i + \text{H.c.}, \tag{A12}$$

where i is the ith waveguide in the array and c_i, $c_i^\dagger$ are the corresponding destruction and creation operators of the ith waveguide mode. Figure 2(b) depicts the quasienergy band structure of the Floquet-Thouless Hamiltonian, which is solved by the quasienergy approach in the Floquet-Bloch theorem [23].

Notably, the tight-binding Hamiltonian is derived from the Westervelt equation (A1) using the approximations of monochromicality, paraxiality, and linearity. With a sound pulse input, however, the monochromic assumption is invalid, so we must return to simulate the dynamics of the linear Westervelt equation (A2), which is the starting point of our FEM simulation of the dynamical Floquet-Thouless pump.

4. The coupling strengths and propagation constants

In order to obtain the coupling strength and propagation constant in our model, we calculate the coupling strength as a function of waveguide spacing d varying from 40 mm to 120 mm, see Fig. 5(a). The coupling strength is extracted from the sound transfer length between two neighboring waveguides. In our experiment, we selected waveguide spacings ranging from 45 mm to 85 mm. We notice that the sound propagation constant depends on the waveguide width. As shown in Fig. 5(b), we calculate the propagation constant for widths varying from 13 mm to 40 mm. In our simulations, our waveguide width ranges from 27 mm to 33 mm.

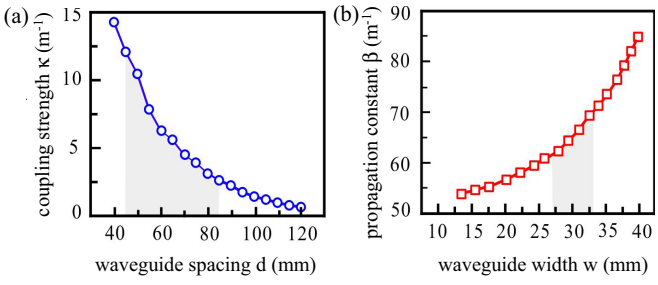

FIG. 5. The propagation constants and coupling strengths as a function of the spacing d between two neighboring waveguides and waveguide width w. (a) For the coupling strengths vs the gap d, we choose the waveguide spacing ranging from 45 to 85 mm. (b) The propagation constant vs the clapboard width w; in our simulations, our waveguide width varies from 27 to 33 mm.

5. Simulation and experiment of incident acoustic wave at the middle position of the initial end of the waveguide at 2900 Hz

To verify the effect of the system on acoustic pumping, as a comparison, we incident an acoustic wave with a frequency of 2900 Hz at the middle position of the initial end of the waveguide, and the simulation and experimental results are shown in Figs. 6(a) and 6(b). From the results, it can be seen that the incident from the middle position does not produce the effect on acoustic pumping.

6. Comparison between experimental data and FEM simulation at the output

To investigate the pumping capability of the system over a broad acoustic frequency range, we conduct experimental measurements and finite-element simulations at two input frequencies of 2850 and 2950 Hz, respectively. As shown in Figs. 7(b) and 7(c), the experimental data and simulations at the output of the tenth Floquet cycle [as shown in Fig. 7(a)] are well matched.

7. Comparisons between pumping zero modes and π modes

The Rice-Mele model is implemented for pumping zero modes by modulating the waveguide width with frequency $\Omega = 2\pi/T$. As shown in Fig. 8(a), the modulation of the width can be described in terms of the propagation constant; in our simulations, our waveguide width varies from 27 to 33 mm. The simulation result depicted in Fig. 8(a) demonstrates that the acoustic energy can be steadily pumped from one side to the other.

Similarly, as depicted in Fig. 8(b), we also designed the π-mode pumping in the array.

8. Thouless pumping of acoustic pulse signal

Figure 9(a) shows a visual comparison of the difference between the π mode and zero modes for pulse signal transmission. Figure 9(b) visually shows its pumping process for a pulse signal. Supplemental Material movie V-4 shows the dynamical pumping over time.

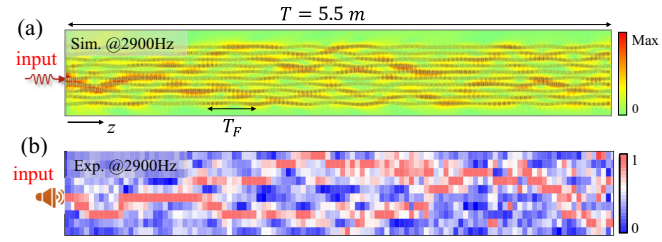

FIG. 6. Simulation and experiments of acoustic waveguide arrays with incident acoustic waves in the middle. (a) Simulation of the propagation effect of the incident acoustic wave in the middle of the waveguide array at 2900 Hz. (b) Experimental measurements of waveguide arrays with intermediate incident acoustic wave propagation at 2900 Hz, with the adiabatic period $T = 5.5$ m and Floquet period $T_F = 0.55$ m.

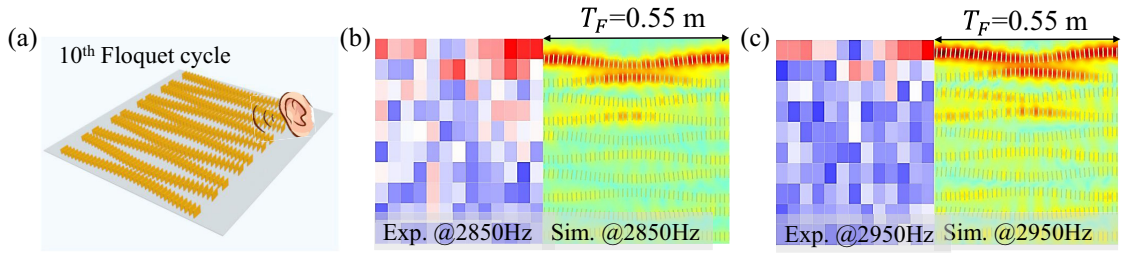

FIG. 7. The experimental data and simulations match well at the output of the last Floquet cycle. (a) The array structure of the tenth Floquet cycle. (b) Comparison between the experimental data and FEM simulation at an input sound frequency of 2850 Hz. (c) Comparison between the experimental data and FEM simulation at an input sound frequency of 2950 Hz.

9. Transmission for different Floquet cycles T_F in an adiabatic cycle T

In the main text, Fig. 4 illustrates that adiabatic evolution at low frequency benefits from longer array lengths for both zero and π mode pumps. However, the π mode pump at high frequency demonstrates nonadiabatic signal transfer over a broader frequency range, providing a distinct advantage over the zero-mode pump. The physical mechanism of the nonadiabatic pump is that, with the frequency modulation by the low-frequency adiabatic modulation and the high-frequency Floquet modulation, as depicted in Fig. 10(a), the fast Floquet modulation serves as the carrier wave in radio telecommunications, while the low-frequency modulation serves as the signal wave. The carrier wave frequency added into the final modulated result allows for conveying the signal pulse with a greater transmission bandwidth. To illustrate the mode evolution clearly, we calculate the pump transmission for an increasing number of Floquet cycles from $n = 4$ to 10, as shown in Figs. 10(c)–10(e), within a fixed adiabatic cycle $T = 3.5$ m.

As reference, we also present the adiabatic pump in Fig. 10(b). The evident high-frequency nonadiabatic pump efficiency arises as the π mode is efficiently supported and subsequently transported from the first waveguide to the tenth, as shown in Figs. 10(d) and 10(e). In contrast, the adiabatic pump efficiency decreases with increasing the Floquet cycles due to the violation of the adiabatic condition in scattering by the modulated waveguides. Specifically, for Floquet cycle number $n = 4$ in Fig. 10(c), we find that the transmission efficiency for both the low-frequency adiabatic pump and the high-frequency nonadiabatic pump is low because the driven condition of the π mode is unsatisfied, and instead, the zero mode is scattered. Near-field distributions at 2.9 and 3.7 kHz are shown in Figs. 10(f)–10(i), further illustrating this point and demonstrating efficient pumping for the high-frequency π mode with increasing Floquet cycle number from $n = 6$ to 10, while at low frequencies, scattering leads to a decrease of transmission efficiency simultaneously.

From the perspective of the waveguide structure characteristic, we can further understand the nonadiabatic Floquet pump. The transmission peak at 2.9 kHz for the adiabatic pump in Fig. 10(b) constrasts with the difficultly in pumping sound at 3.7 kHz. The physical mechanism involves periodic sheets creating acoustic waveguides that strongly constrain sound propagation along the waveguides while offering weaker coupling between adjacent waveguides for higher-frequency incident sound.

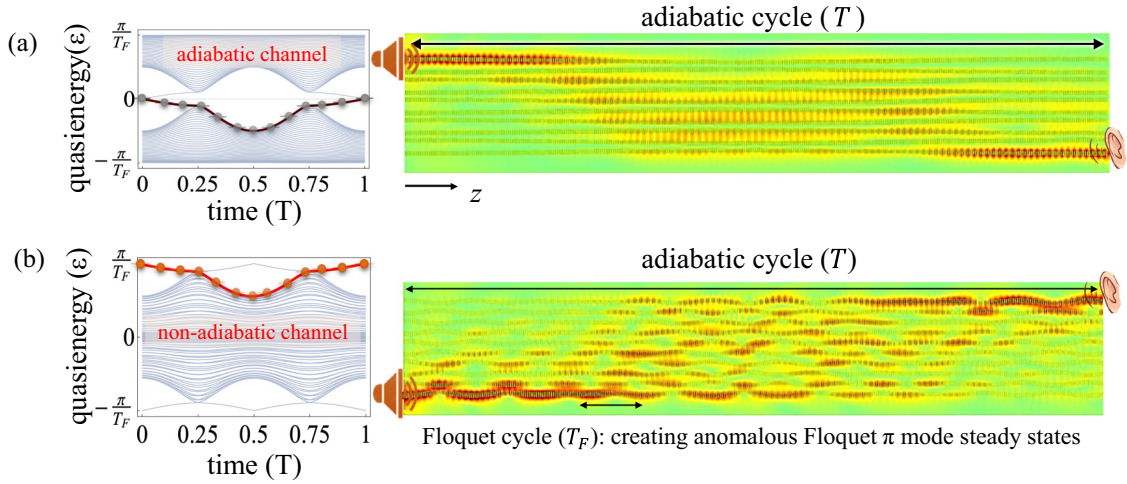

FIG. 8. Comparisons between pumping zero modes and π modes. (a) The Thouless pump (zero modes) channels in the quasienergy spectrum and the FEM simulation of the adiabatic Thouless pump (i.e., zero-mode pump) based on the Rice-Mele model. (b) The Floquet-Thouless pump (π modes) channels in the quasienergy spectrum and the FEM simulation of the Floquet-Thouless pump (i.e., π mode pump) on the acoustic waveguide array.

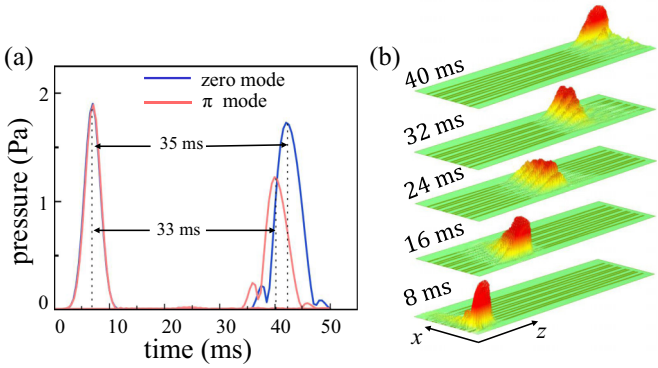

FIG. 9. Adiabatic Thouless pumping of the acoustic pulse signal. (a) Comparison of zero-mode pumping and Floquet π mode for pulse signal transmission. (b) Simulation diagram of a pulse pumping in the zero-mode pump channel.

Consequently, sound at 2.9 kHz couples more easily between adjacent waveguides and pumps to the tenth waveguide in the adiabatic period $T = 3.5$ m, as shown in Fig. 10(f). However, at 3.7 kHz, the sound remains tightly bound to its original waveguide, with minimal coupling occurring only midway, leaving insufficient distance to pump the sound to the tenth waveguide within $T = 3.5$ m, as shown in Figs. 10(f) and 10(l).

Introducing Floquet modulation with the Floquet cycle $T_F = T/4$ decreases the transmission for both low adiabatic frequency and high nonadiabatic frequency, as shown in Fig. 10(c). This occurs because the adiabatic condition is disrupted for the adiabatic pump, and the π mode is not yet excited. This process can be observed in the near fields [Fig. 10(g)] and in the waveguide structure [Fig. 10(k)]. Increasing the modulation to a Floquet cycle of $T_F = T/6$ effectively excites the π mode at incident frequencies of 2.9 and 3.7 kHz, resulting in high pumping transmissions [Fig. 10(d)].

In the adiabatic frequency region, the near field presented in Fig. 10(h) shows that sound at 2.9 kHz begins pumping in the tremble region 1 [outlined in Fig. 10(l)], traversing through tremble region 2 to be entirely pumped to the other edge over $T = 3.5$ m. Conversely, in the nonadiabatic frequency region, sound at 3.7 kHz faces difficultly in pumping within the first tremble region due to short tremble distance and strong binding. However, it is quickly pumped to the other edge in tremble region 2, as shown in Fig. 10(h), differing from the adiabatic pump in Fig. 10(f).

To achieve the Thouless pump in shorter lengths, we increase the tremble strength to the Floquet cycle of $T_F = T/10$. This enhances the efficiency of the nonadiabatic pump at high frequencies, shortening the pump and transfer length, as shown in Fig. 10(i). Comparing the practical waveguide structures in Figs. 10(j)–10(m), we observe that the Floquet modulation provides more coupling and pumping

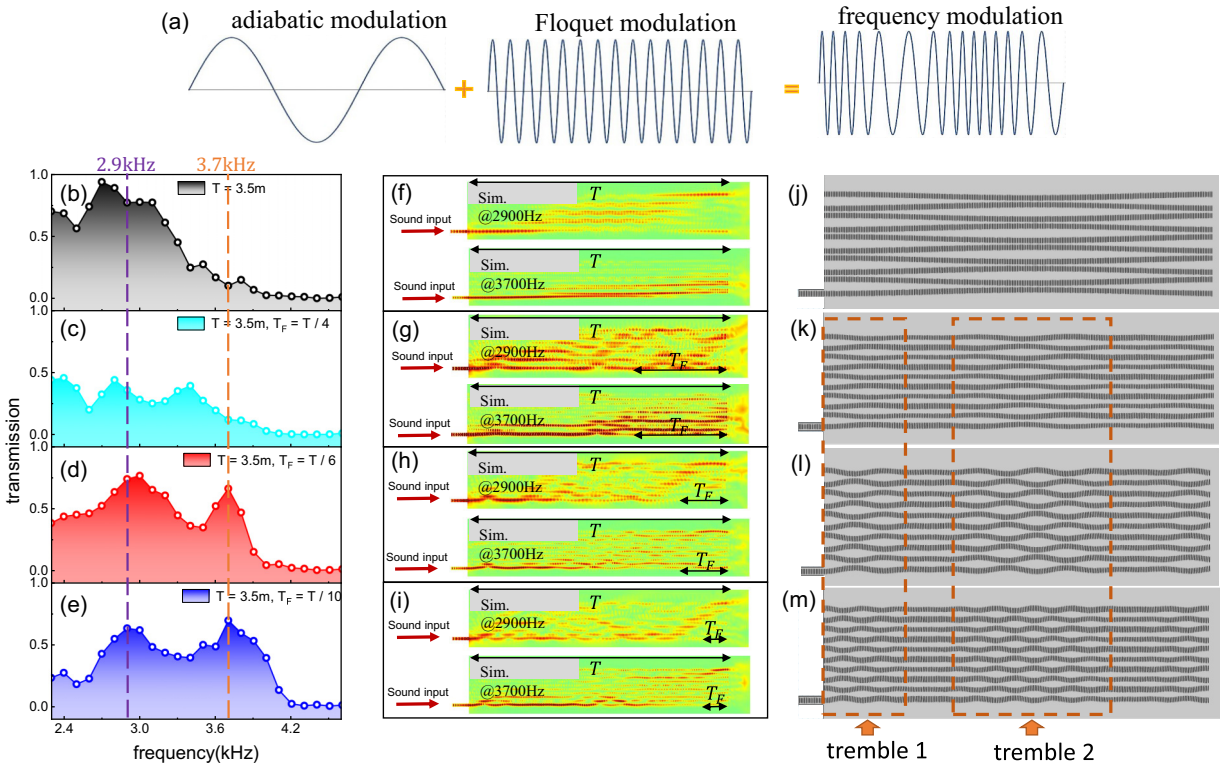

FIG. 10. (a) Analogous explanation of the Floquet-Thouless pump with frequency modulation schemes. Transmission of adiabatic and nonadiabatic pumps for different Floquet cycle number in a fixed adiabatic cycle $T = 3.5$ m with $T_F = T/4$, $T_F = T/6$, and $T_F = T/10$ shown in (c), (d), and (e); as a reference, the adiabatic pump is shown in (b). Specifically, (c) shows neither adiabatic nor nonadiabatic pump feature, because at this moment the adiabatic condition is broken for adiabatic pump while the π mode has not been excited yet. (f)–(i) correspond to the near-field distributions at incident frequency as 2900 and 3700 Hz. (j)–(m) correspond to the practical waveguide structures.

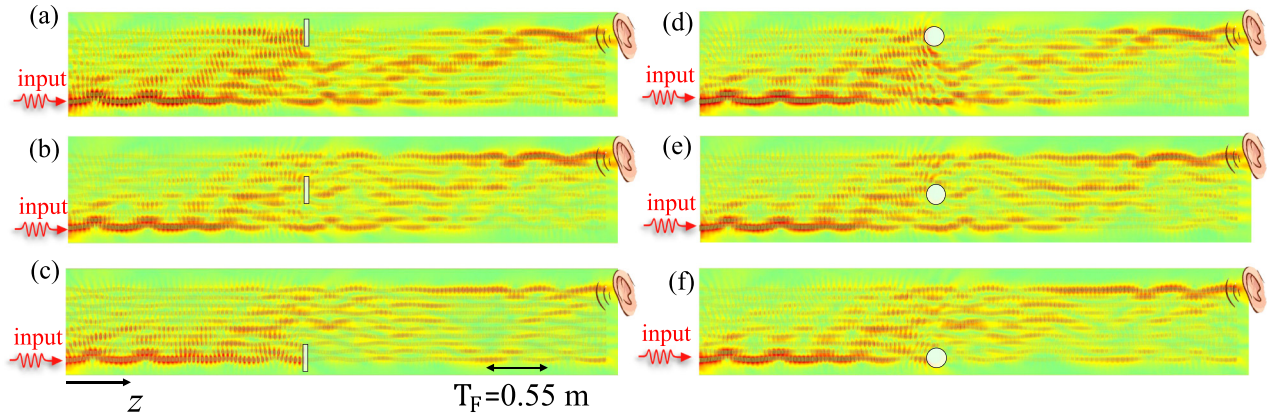

FIG. 11. Protection of the Floquet-Thouless pump against defects with the input of continuous waves at a frequency of 2900 Hz. (a)–(c) A defect consisting of a hard, square partition with a height of 150 mm and a width of 20 mm is placed at different spatial locations of the array. (d)–(f) A defect consisting of hard, circular blocks with a radius of 35 mm is placed. As compared with Fig. 3, we show that the acoustic array can pump both continuous and pulsed waves, indicating the capability of energy and information transfer in acoustics.

opportunities in tremble regions, thereby shortening the pump length.

10. Robustness against defects in Floquet-Thouless pump

Next, to assess the topological protection of our acoustic Floquet-Thouless pump system, we positioned a hard square partition of 150 mm × 20 mm at different locations along the waveguide array. As depicted in Figs. 11(a)–11(c), acoustic energy can be successfully pumped to the output waveguide. Similarly, in Figs. 11(d)–11(f), rigid circles of 35 mm radius are positioned in the center of the array, and then we observe that the majority of the sound intensity can be pumped effectively. Still, a small portion of the acoustic wave is scattered by the circles, indicating the protection capability depends on the defect structures. Nonetheless, we can still summarize that our acoustic waveguide system for the nonadiabatic pump is topologically shielded and has a high level of defect immunity.

Also, we further investigate the robustness of temporal dynamical pumping, as shown in Figs. 12(a) and 12(b). We find that the pulsed sound can easily pass across the defect and fully reconstruct itself at the end output of the array. This protected dynamical pumping of sound pulse resembles an acoustic cloaking process that may be utilized in signal transfer and wave manipulation of sound.

11. Movies

We create several movies to demonstrate the dynamical Floquet-Thouless pumping of sound pulse (see Supplemental Material [28]).

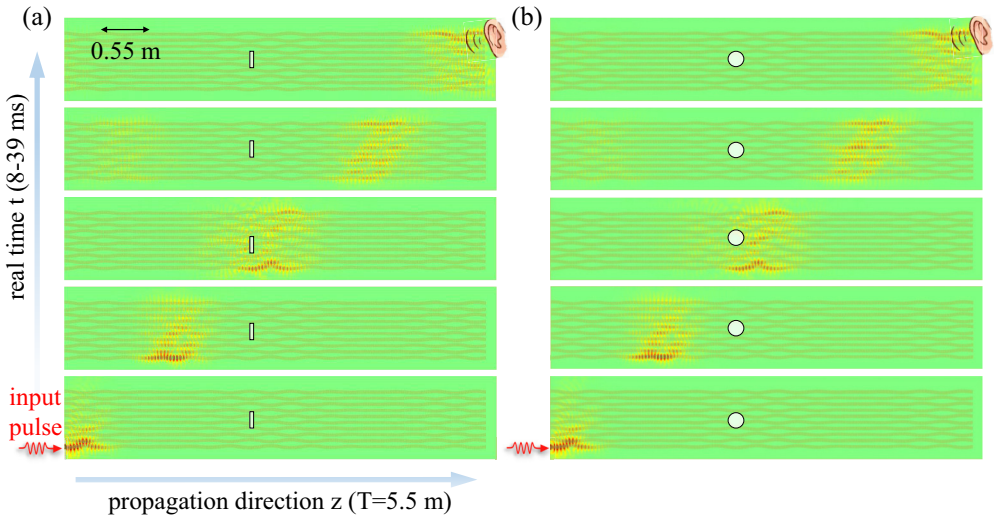

FIG. 12. Protection of the dynamical Floquet-Thouless signal pump against defects. (a) A defect consisting of a hard, square partition with a height of 150 mm and a width of 20 mm is placed at the center of the array. (b) A defect consisting of hard, circular blocks with a radius of 35 mm is placed at the center. The pump channel demonstrates considerable immunity to backscattering from these defects in both cases.

[1] Q. Niu and D. J. Thouless, Quantised adiabatic charge transport in the presence of substrate disorder and many-body interaction, J. Phys. A: Math. Gen. **17**, 2453 (1984).

[2] D. J. Thouless, Quantization of particle transport, Phys. Rev. B **27**, 6083 (1983).

[3] Y. E. Kraus, Y. Lahini, Z. Ringel, M. Verbin, and O. Zilberberg, Topological states and adiabatic pumping in quasicrystals, Phys. Rev. Lett. **109**, 106402 (2012).

[4] M. Lohse, C. Schweizer, O. Zilberberg, M. Aidelsburger, and I. Bloch, A Thouless quantum pump with ultracold bosonic atoms in an optical superlattice, Nat. Phys. **12**, 350 (2016).

[5] O. Zilberberg, S. Huang, J. Guglielmon, M. Wang, K. P. Chen, Y. E. Kraus, and M. C. Rechtsman, Photonic topological boundary pumping as a probe of 4D quantum Hall physics, Nature (London) **553**, 59 (2018).

[6] M. Verbin, O. Zilberberg, Y. Lahini, Y. E. Kraus, and Y. Silberberg, Topological pumping over a photonic Fibonacci quasicrystal, Phys. Rev. B **91**, 064201 (2015).

[7] Y. Ke, X. Qin, F. Mei, H. Zhong, Y. S. Kivshar, and C. Lee, Topological phase transitions and Thouless pumping of light in photonic waveguide arrays, Laser Photonics Rev. **10**, 995 (2016).

[8] A. Cerjan, M. Wang, S. Huang, K. P. Chen, and M. C. Rechtsman, Thouless pumping in disordered photonic systems, Light. Sci. Appl. **9**, 178 (2020).

[9] H. Chen, H. Zhang, Q. Wu, Y. Huang, H. Nguyen, E. Prodan, X. Zhou, and G. Huang, Creating synthetic spaces for higher-order topological sound transport, Nat. Commun. **12**, 5028 (2021).

[10] X. Xu, Q. Wu, H. Chen, H. Nassar, Y. Chen, A. Norris, M. R. Haberman, and G. Huang, Physical observation of a robust acoustic pumping in waveguides with dynamic boundary, Phys. Rev. Lett. **125**, 253901 (2020).

[11] Z. G. Chen, W. Tang, R. Y. Zhang, Z. Chen, and G. Ma, Landau-Zener transition in the dynamic transfer of acoustic topological states, Phys. Rev. Lett. **126**, 054301 (2021).

[12] W. Cheng, E. Prodan, and C. Prodan, Experimental demonstration of dynamic topological pumping across incommensurate bilayered acoustic metamaterials, Phys. Rev. Lett. **125**, 224301 (2020).

[13] Y. Long and J. Ren, Floquet topological acoustic resonators and acoustic Thouless pumping, J. Acoust. Soc. Am. **146**, 742 (2019).

[14] Y. Xia, E. Riva, M. I. N. Rosa, G. Cazzulani, A. Erturk, F. Braghin, and M. Ruzzene, Experimental observation of temporal pumping in electromechanical waveguides, Phys. Rev. Lett. **126**, 095501 (2021).

[15] I. H. Grinberg, M. Lin, C. Harris, W. A. Benalcazar, C. W. Peterson, T. L. Hughes, and G. Bahl, Robust temporal pumping in a magneto-mechanical topological insulator, Nat. Commun. **11**, 974 (2020).

[16] Z. Fedorova, H. Qiu, S. Linden, and J. Kroha, Observation of topological transport quantization by dissipation in fast Thouless pumps, Nat. Commun. **11**, 3758 (2020).

[17] T. Ozawa *et al.*, Topological photonics, Rev. Mod. Phys. **91**, 015006 (2019).

[18] I. L. Garanovich, S. Longhi, A. A. Sukhorukov, and Y. S. Kivshar, Light propagation and localization in modulated photonic lattices and waveguides, Phys. Rep. **518**, 1 (2012).

[19] Y. X. Shen, L. S. Zeng, Z. G. Geng, D. G. Zhao, Y. G. Peng, and X. F. Zhu, Acoustic adiabatic propagation based on topological pumping in a coupled multicavity chain lattice, Phys. Rev. Appl. **14**, 014043 (2020).

[20] Z. Chen, Z. Chen, Z. Li, B. Liang, G. Ma, Y. Lu, and J. Cheng, Topological pumping in acoustic waveguide arrays with hopping modulation, New J. Phys. **24**, 013004 (2022).

[21] Y. G. Peng, Z. G. Geng, and X. F. Zhu, Topologically protected bound states in one-dimensional Floquet acoustic waveguide systems, J. Appl. Phys. **123**, 091716 (2018).

[22] F. Liu, S. Ghosh, and Y. D. Chong, Localization and adiabatic pumping in a generalized Aubry-André-Harper model, Phys. Rev. B **91**, 014108 (2015).

[23] Y. Pan, A. Dikopoltsev, E. Lustig, Q. Cheng, and M. Segev, Anomalous Floquet Thouless pumping, in *Conference on Lasers and Electro-Optics (CLEO)* (IEEE, New York, 2021).

[24] M. F. Hamilton and D. T. Blackstock, *Nonlinear Acoustics* (Academic Press, New York, 1997).

[25] S. Longhi, Quantum-optical analogies using photonic structures, Laser Photonics Rev. **3**, 243 (2009).

[26] M. J. Rice and E. J. Mele, Elementary excitations of a linearly conjugated diatomic polymer, Phys. Rev. Lett. **49**, 1455 (1982).

[27] Q. Cheng, H. Wang, Y. Ke, T. Chen, Y. Yu, Y. S. Kivshar, C. Lee, and Y. Pan, Asymmetric topological pumping in nonparaxial photonics, Nat. Commun. **13**, 249 (2022).

[28] See Supplemental Material at http://link.aps.org/supplemental/10.1103/PhysRevB.110.085137 for brief description on Floquet-Thouless pumping dynamics of sound waves.